IEEE Open Journal of Antennas and Propagation

Received XX August, 2024; revised XX Month, XXXX; accepted XX Month, XXXX; Date of publication XX Month, XXXX; date of current version XX Month, XXXX.

Digital Object Identifier 10.1109/OJAP.20xx.1234567

Dual-Polarized Wideband Filtering Antenna Array Based on Stacked-PCB Structure

MATTI KUOSMANEN[1,2], STEN E. GUNNARSSON[3] (Senior member, IEEE), JOHAN MALMSTRÖM[3] (Member, IEEE), JUHA ALA-LAURINAHO[2], JARI HOLOPAINEN[2], AND VILLE VIIKARI[2] (Senior member, IEEE)

[1]Saab Finland Oy, 00100 Helsinki, Finland
[2]Department of Electronics and Nanoengineering, Aalto University, 02150 Espoo, Finland
[3]Saab AB, Nettovägen 6, SE-175 88 Järfälla, Sweden

CORRESPONDING AUTHOR: Matti Kuosmanen (e-mail: matti.s.kuosmanen@aalto.fi).

This work was funded by Saab AB. The work of Matti Kuosmanen was supported by Finnish Foundation for Technology Promotion and Walter Ahlström Foundation.

ABSTRACT This paper investigates a thin low-pass filtering antenna array based on dual-polarized Vivaldi elements. The low-pass filtering in the antenna elements reduces the requirement for the front-end filtering between the antenna and the microwave electronics, resulting in improved overall out-of-band suppression, size reduction, and lower cost. The array employs a novel stacked-PCB structure, where simple two-sided PCBs are stacked on top of each other. The via-connected metal layers of all PCBs form a tapered slotline along the surface normal of the PCBs. The filtering effect is realized by corrugating the tapered slotlines, which provides effective, space-saving integration of the filters that fit into a half-wavelength lattice. According to unit-cell simulations, the proposed antenna array operates at 6–18.5 GHz, and the stopband extends from 21 GHz to 37 GHz. The antenna array provides a −10-dB active reflection coefficient (ARC) with beam-steering angles within ±60° in E- and D-planes, and −6 dB within ±55° in the H-plane. At stopband frequencies, the attenuation with respect to simulated total efficiency is at least 20 dB. The operation of the proposed antenna array is confirmed by measurements of an 11×12 antenna array prototype, which show that the gain suppression level in the stopband is more than 30 dB up to 37 GHz, and more than 20 dB up to 40 GHz.

INDEX TERMS antenna array, filtenna, filtering antenna, flared notch, periodic slotline, planar, printed circuit board (PCB), tapered slotline, Vivaldi

I. INTRODUCTION

MANY wireless systems employ antenna arrays to agilely direct the microwave energy in the desired direction. This effect is exploited, for example, in radar systems and mobile communications. In these radio systems, the antenna arrays are the outermost part of the signal chain. Before the antenna array, the signal chain includes several filters, which filter out both unintentional spurious emissions in transmission and interfering signals from the environment in reception. Usually, filters are external microwave components associated with a relatively high cost and size if high-Q performance is required.

To improve the compactness and overall performance of the radio system, the integration of front-end filtering functions into antennas and antenna arrays has attracted increasing interest among researchers. Incorporating at least a part of the filtering function into the antenna itself might not only improve the filtering properties but also lower cost and reduce the overall size as cheaper or lower-order filter technology can be employed in other parts of the signal chain.

A common method to integrate a filter to the antenna array is to place it into the feeding network (e.g., [1]–[3]), where it is possible to use transmission line filters. Another approach is to integrate individual filters into each

This work is licensed under a Creative Commons Attribution 4.0 License. For more information, see https://creativecommons.org/licenses/by/4.0/

antenna element, which has been done, for example, in [4]–[6]. In many cases, both the properties of antenna elements and feed network are considered in the design process, and the resulting filtering response depends on both parts (e.g., [7], [8]). The approach of individual filters is particularly feasible for active, beam-steerable antenna arrays, as the feeding arrangement or excitation coefficients do not affect the filtering response.

In this paper, we present a planar Vivaldi-based filtering antenna, which employs a corrugated slotline to provide low-pass filtering. The operational band of the antenna is 6–18.5 GHz and the stopband extends from 21 GHz to 37 GHz. The antenna is constructed of several stacked two-layer PCBs, which are galvanically connected to each other by mechanical pressure using screws. The copper layers and connecting vias of each PCB form a tapered slotline inside the PCB stack such that the slotline opens to the direction of the surface normal. The sizes of the copper pads and the placement of connecting vias are altered such that the slotline is corrugated. This corrugation forms a periodic transmission line that acts as a filter, as previously studied in [9].

The filtering properties of periodic transmission lines have been exploited for decades [10], [11]. In tapered slotline antennas, this is a particularly suitable method for filter integration for several reasons. First, the periodicity is straightforward to implement in a slotline by adding short-circuited stubs. Moreover, the dense spacing of stubs makes the filtering method ideal for a steep, space-saving filter integration. By filling the stubs with dielectric material, the physical length of the stubs is reduced, and they can be fitted into a conventional half-wavelength antenna array lattice. Thus, every antenna element in a dense array can be equipped with a filter, which is crucial in modern active arrays.

To the authors' knowledge, this is the first fully planar, dual-polarized Vivaldi array that is constructed by stacking several PCBs as layers to build the array structure. In contrast to the conventional PCB-based Vivaldi arrays, the radiation direction of the array is perpendicular to the PCB surface, as illustrated in Fig. 1. Furthermore, the proposed structure enables the integration of low-pass filter characteristics in the antenna element.

The low-loss PCB substrates cause dielectric loading into the Vivaldi slot, which helps to reduce the height of the array [12]. Moreover, the stacked structure enables the use of different PCB materials which can be used to improve the impedance matching of the antenna elements. Notably, this particular construction method is useful also for non-filtering arrays. In that case, the Vivaldi slot is not corrugated and the whole array can be made of only a few, thicker PCBs, which makes the construction of the array simple.

Most of the filtering antenna arrays presented in the literature include relatively narrow band-pass filtering functions that are suitable especially for telecommunication purposes. The proposed antenna array, however, has a large bandwidth

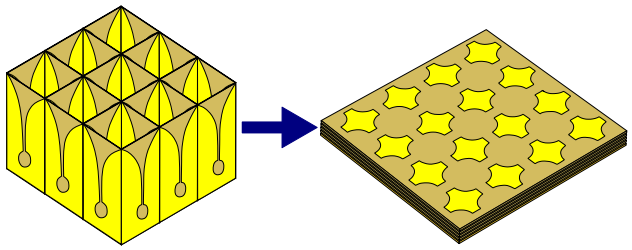

FIGURE 1. Illustration of the proposed planar Vivaldi array concept. Instead of conventional PCB-based Vivaldi array in an egg-crate lattice (left), the Vivaldi elements are constructed inside the stack of planar PCBs (right).

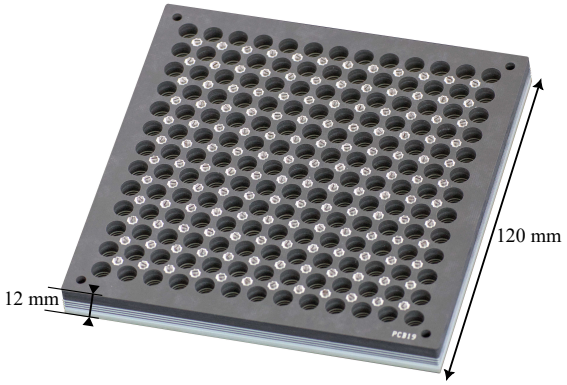

FIGURE 2. Photograph of the manufactured 11×12 antenna array.

and low-pass functionality. A large bandwidth is needed, for example, in modern signal intelligence receivers, cognitive radars, and multifunctional systems. In reception, the low-pass filter helps to suppress high-frequency out-of-band signals. In transmission, the low-pass filter suppresses the harmonic distortion components of the transmitter [13]. The low-pass filtering arrays have also been used to decrease the coupling between the low-band and high-band antenna elements in base station antenna arrays [14].

The rest of the paper is structured as follows: First, the background theory behind the integrated filtering is briefly described. Second, antenna structure is described in detail. Then, the antenna array is analyzed by unit-cell simulations. After that, the full-array measurement results of the manufactured 11×12 array [Fig. 2] are presented and compared to the unit-cell and full-array predictions. Finally, the paper summarizes the outcomes of the study and concludes.

II. ANTENNA STRUCTURE AND OPERATING PRINCIPLE

A. BACKGROUND THEORY

The filtering effect of the antenna elements is based on a periodically loaded slotline. It means that both branches of the conventional slotline are loaded by series impedance elements that are placed densely with respect to the wavelength. The periodic loading on the transmission line (TL) cause special dispersion properties that differ from the conventional unloaded TL. Thus, the transmission line has also periodic

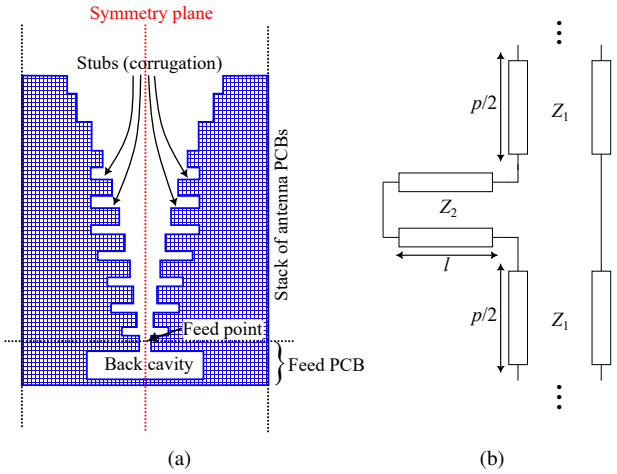

FIGURE 3. (a) Simplified cross-section of the proposed antenna array element showing a periodic stub-loaded slotline. The red line shows the symmetry plane. (b) Unit-cell circuit model of the stub-loaded transmission line. The circuit corresponds to one segment of periodically loaded slotline. Adapted from [9].

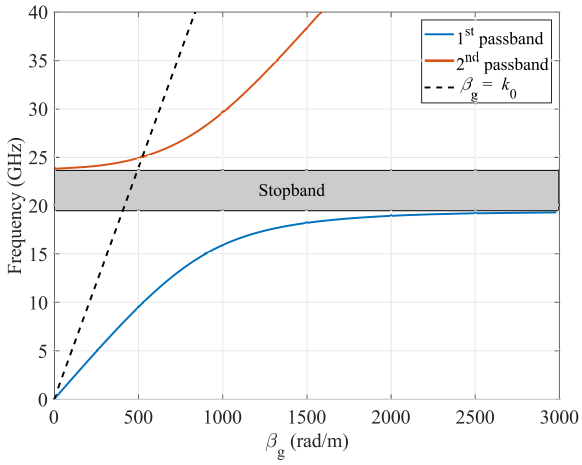

FIGURE 4. Dispersion diagram of the ideal, uniform stub-loaded transmission line of Fig. 3. The dashed line ($\beta_g = k_0$) shows the behaviour of an unloaded TEM transmission line.

transmission properties and cut-off frequencies that depend on the configuration of the periodic loading [10].

In the proposed antenna array, the periodic loading of the slotline is realized by short-circuited series stubs, i.e., corrugation. The cross section of the physical structure showing a plurality of stubs in a Vivaldi slot is shown in Fig. 3 (a). The corresponding TL model of one unit cell is shown in Fig. 3 (b). However, only one branch is illustrated in the TL model as the effect of the second branch can be easily understood by the image principle. Series stubs cause dispersion that strongly increases near the cut-off frequency of the TL. The relation of the guided wavelength λ_g in the loaded TL and the wavelength of the unloaded TL λ_1 is given by [10]

$$\cos\frac{2\pi p}{\lambda_g} = \cos\frac{2\pi p}{\lambda_1} - \frac{Z_2}{2Z_1}\tan\frac{2\pi l}{\lambda_2}\sin\frac{2\pi p}{\lambda_1}, \qquad (1)$$

where Z_1 and Z_2 are the characteristic impedances of the unloaded transmission line and the stub, respectively, λ_2 is the wavelength in the stub, p is the period, and l is the length of the stub. The first cut-off frequency occurs when $\lambda_g = 2p$ and it is slightly smaller than the quarter-wavelength frequency of the stub [10].

Based on (1), the frequency of the guided wave with respect to the wave number $\beta_g = 2\pi/\lambda_g$ is plotted in Fig. 4. This dispersion curve is computed by assuming that $Z_2/Z_1 = 0.32$, $p = 1.054$ mm, $l = 1.5$ mm, $\lambda_1 = \sqrt{3.6}\lambda_0$, and $\lambda_2 = \sqrt{6.15}\lambda_0$, λ_0 being the wavelength in free space. These values have been estimated from the proposed antenna structure shown in Figs. 3 (a) and 5. At the cut-off frequency (19 GHz), which is mainly defined by the length of the stub, λ_g approaches zero and the wave stops propagating. That is, β_g approaches infinity. This dispersion property of the periodically loaded TL causes a low-pass filtering phenomenon with a steep transition band. There is also an additional passband at higher frequencies (starting at 24 GHz) which comes from the periodic nature of the transmission line. However, if stubs of different lengths are embedded in the transmission line, the extra passbands are effectively suppressed. Note that Fig. 4 is a simplified example on the properties of the periodically loaded transmission line, and it does not fully describe the properties of the proposed antenna array.

To summarize, the slotline loaded with short-circuited stubs can be treated as a periodic transmission line. The corrugated slotline causes dispersion characterized by (1), and the dispersion property causes a low-pass filtering phenomenon. The cut-off frequency of the stub-loaded slotline is mainly defined by the length of the stub, as it can be found inside the tangent function in (1). This is also the parameter that can be used to tune the cut-off frequency during the design process. More sophisticated analysis on periodic TLs can be found in [9]–[11].

B. ANTENNA STRUCTURE

The antenna structure consists of 19 two-layer PCBs and one four-layer PCB, which are stacked on top of each other. The two-layer PCBs form the radiating slot, and the four-layer PCB acts as the feed PCB which contains baluns and connectors. All PCBs have an immersion silver surface finish.

1) FEED PCB

The four-layer feed PCB is made of Rogers RO4350B laminate ($\epsilon_r = 3.66$, $\tan\delta = 0.0037$ at 10 GHz) and RO4450F bondplies ($\epsilon_r = 3.52$, $\tan\delta = 0.004$ at 10 GHz). In Figs. 5 and 6 the detailed structure of the feed PCB is presented. The signal is fed through a C.FL connector [15] and a microstrip line to the balun structure, which consists of a signal via, stripline, ground vias, and back-cavity inside

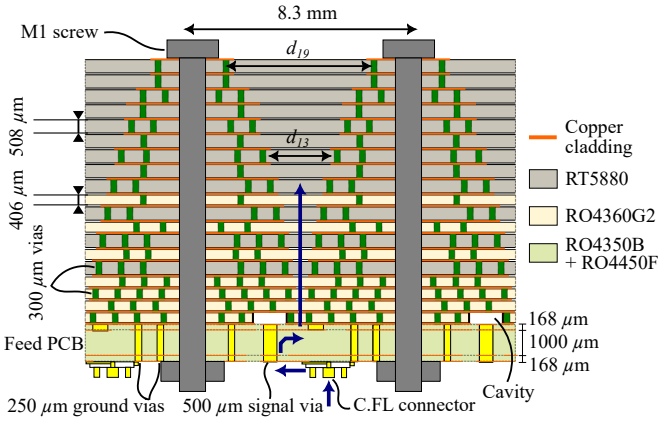

FIGURE 5. **Detailed cross-section of the proposed antenna array. Only one antenna element is illustrated. The green vias are not visible in the real cross-section as they are offset from the center line. However, they illustrate the indentations in the tapered slotline. Blue arrows show the signal propagation direction through the structure. Antenna PCBs (on the top of the feed PCB) are numbered 1–19, starting from the bottom.**

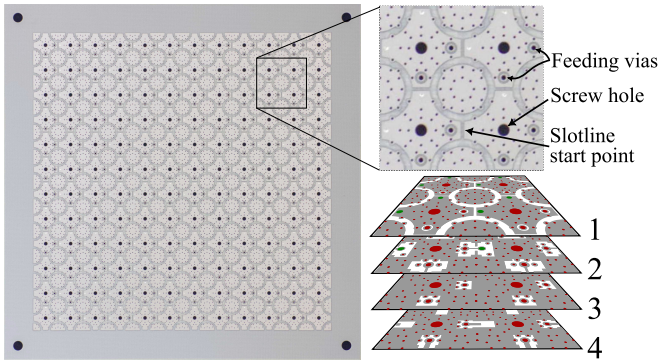

FIGURE 6. **The top side (against the antenna PCBs) of the feed PCB and all four layers of the PCB. Red dots are PTHs and green dots are blind vias between layers 1 and 2.**

the PCB. The blue arrows in Fig. 5 show the path for the signal from the C.FL connector to the radiating slot.

As shown in Fig. 6, the first and second layers (from the top) are heavily filled with copper. The main idea is to prevent the radiation of the feed PCB: if there were large, non-conductive areas on the PCB, the fields inside the feed PCB would radiate. The antenna structure above the feed PCB would not prevent this radiation as there are big holes between the antenna elements. Similar feed PCB, without radiation-preventing mechanisms, was successfully used also in [12], [16].

2) ANTENNA PCBS

The 19 different two-layer antenna PCBs are made of Rogers RO4360G2 ($\epsilon_r = 6.15$, $\tan\delta = 0.0038$ at 10 GHz) and Rogers RT/Duroid 5880 ($\epsilon_r = 2.20$, $\tan\delta = 0.0009$ at 10 GHz) substrates. The layout of the first PCB (on the top of the feed PCB) is shown in Fig. 7. The PCB layout contains cross-shaped copper pads on both sides, and they are connected together by vias. The empty areas between the cross-shaped pads are perforated by 6.5-mm holes. In the center of the copper pads, there are 1.2-mm plated through holes (PTH) for the screws. In this first (bottom) antenna PCB, there is also an additional 1.0-mm PTH which creates a cavity on the top of the feeding via of the feed PCB and prevents its short circuit. The short circuit of the feed via can be avoided also by other methods, such as the back-drilling process (the top part of the PTH is drilled off) or using blind vias. However, these special features usually cost more and add special restrictions for via diameter and depth.

The two-layer antenna PCBs are stacked as shown in Fig. 5, and the cross-shaped pads of all PCBs are in galvanic contact with each other. The shape of the copper pads of all antenna PCBs is similar, but the gap between the adjacent copper pad vias (d_n, $n = 1 \ldots 19$) increases according to Table 1 along the broadside direction. Obviously, the placement of the small vias is altered as the copper pads become smaller. The vias are placed as close to the copper pad edges as possible: in this design, the clearance from the via to the edge is 0.125 mm. The perforation and the PTHs for the screws remain identical throughout the whole stack. Fig. 8 further illustrates the tapered shape of the antenna elements when the PCB substrate is hidden.

As the PCBs contain fine details and the gaps between the cross-shaped pads are narrow, the proper alignment of the PCBs is crucial. When the prototype was manufactured, the alignment of all layers was done by inserting a few alignment pins into non-plated holes that go through the stack of PCBs. After the screws were fastened, alignment pins were removed. The used technique was shown to provide a proper alignment since all measured elements worked as expected.

The proposed antenna array uses cross-shaped copper pads but also other shapes are possible. For example, the circular copper pads would result in body-of-revolution (BoR) elements which are used in wideband antenna arrays [17]. However, based on our experience, BoR-shaped filtering elements do not provide as good filtering properties as the cross-shaped ones since the frequency response of filtering BoR elements depends on the beam-steering angle.

The antenna PCBs are made of high- and low-permittivity substrate materials. The high-permittivity substrate is needed to provide electrically longer stubs: As the filter cut-off occurs when the electrical length of the stub is near a quarter wavelength, the high-permittivity material is needed in order to fit the stubs inside a half-wavelength square lattice of the antenna elements. In turn, the low-permittivity material improves the impedance matching and surface-wave rejection of the antenna array. When the permittivity of the stack decreases gradually along the broadside direction, the impedance matching of the electromagnetic wave from the antenna to the free space is improved. Furthermore, the use of low-permittivity material in conjunction with perforation effectively prevents the propagation of surface waves along the antenna array [18], [19].

This article has been accepted for publication in IEEE Open Journal of Antennas and Propagation. This is the author's version which has not been fully edited and content may change prior to final publication. Citation information: DOI 10.1109/OJAP.2024.3466234

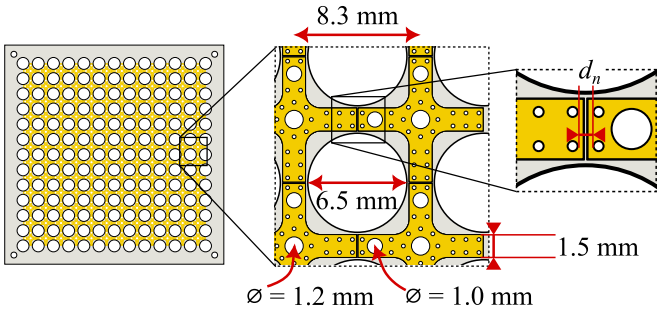

FIGURE 7. The bottom layer of the first antenna PCB on top of the feed PCB. The zoomed picture on the right shows the details and relevant dimensions of the antenna structure. Dimensions d_n are shown in Table 1.

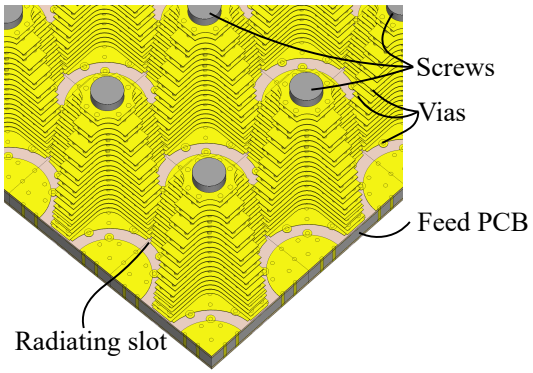

FIGURE 8. Perspective view of the antenna array when the substrate material of the antenna layers is hidden. All yellow parts represent copper layers and vias.

In [9], the filtering antenna element based on a similar periodically loaded transmission line was surrounded by a waveguide. The reason for this kind of shielding was to add the high-pass filter functionality and to prevent the radiation of the periodic slotline. The results indicate that the effect of the waveguide is crucial regarding the filtering performance. However, in this paper, we do not have any waveguide or other shielding structure around the slotline. The main reason for the successful operation without a waveguide is the better confinement of fields inside the slotline. That is, the Vivaldi flares are thicker than those in the standard Vivaldi-antenna based on a single PCB, and the slot is fully filled by (high-permittivity) dielectric material.

III. UNIT-CELL SIMULATIONS

The unit-cell simulations were conducted in CST Studio Suite 2023 using unit-cell boundary condition that corresponds an infinite array approximation. Three sets of results are shown: active reflection/coupling coefficients (ARC/ACC), embedded-element patterns (EEPs), and total efficiencies. As the finite-array performance differs quite much from the infinite-array predictions, the performance characteristics are evaluated based on the unit-cell simulations. This approach gives a fair comparison between different antenna array designs.

TABLE 1. Distance between the edge vias of adjacent cross-shaped copper pads (d_n). The distance is defined as the closest dimension between the via edges. The gap between the metal layers is respectively 250 μm smaller (125 μm clearance between the via and metal edge).

Parameter	Value (mm)	Parameter	Value (mm)
d_1	0.350	d_{11}	1.95
d_2	1.76	d_{12}	4.25
d_3	0.561	d_{13}	2.55
d_4	2.62	d_{14}	4.25
d_5	0.817	d_{15}	3.30
d_6	2.93	d_{16}	4.21
d_7	1.13	d_{17}	4.21
d_8	3.70	d_{18}	5.34
d_9	1.50	d_{19}	5.34
d_{10}	4.25		

A. ACTIVE REFLECTION AND COUPLING COEFFICIENTS

The simulated active reflection coefficient of an infinite array is presented in Fig. 9. In the E-plane, the coupling of the elements is strong which enables the wideband operation in a large beam-steering range of $\pm 60°$ with ARC < -10 dB. However, in the H-plane, the array behaves differently and the ARC rises up to -6 dB. In the D-plane, the ARC is mainly somewhere between the values of E- and H-plane ARCs.

When the ARC of an infinite array is compared to other published Vivaldi arrays, e.g., [12], it is worse in the H-plane. This effect is probably due to the slotted edge of the Vivaldi element and the different permittivity-reduction method. In this work, perforations are outside the radiating slot, which is probably not as good method as that of [12]. One should still note that the ARCs are usually worse in the H-plane if the antenna array elements are tightly coupled or connected. This phenomenon is shown, e.g., in [9], [19].

The simulated active coupling coefficient in the D-plane is shown in Fig. 10. The results are typical for a Vivaldi array of this height [12], [20]. In E- and H-planes, the coupling is negligible and not shown here.

B. EMBEDDED-ELEMENT PATTERNS

The embedded-element patterns of the infinite array are shown in Fig. 11. Both co- and cross-polarized components are given based on Ludwig's third definition [21]. The results are given at three different frequencies, and they reveal very predictable behavior over the operational bandwidth. At the lowest frequency (6 GHz), the scan-loss and cross-polarization levels are minimal, as can be concluded from the simulated ARC and the height of the antenna element. When the frequency increases, the cross-polarization levels increase and scan loss gets worse. At the highest frequency, the maximum cross-polarization level in the D-plane is just a couple of decibels lower than the co-polarization levels, which indicates that the antenna element height has become large in wavelengths. At all frequencies, there is

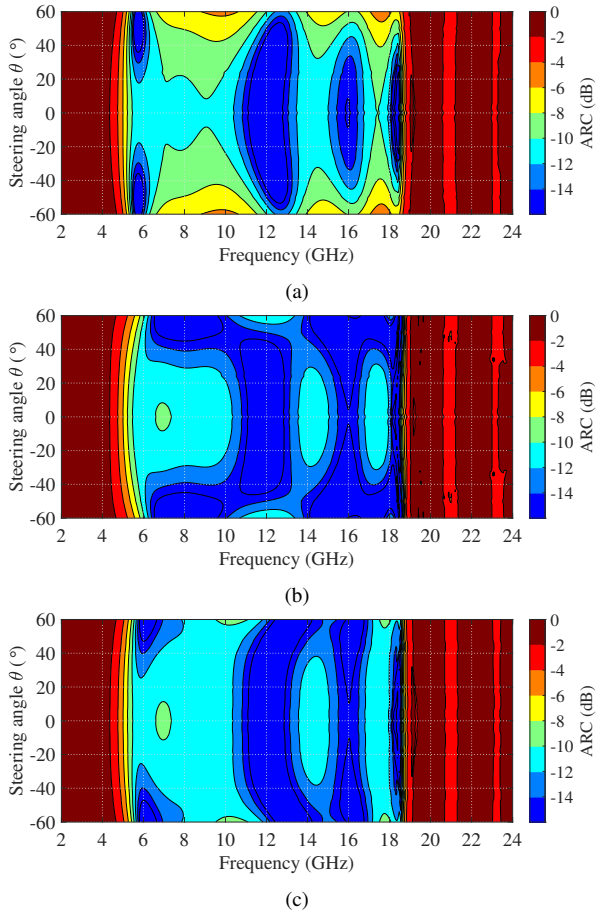

FIGURE 9. **Simulated active reflection coefficient of the infinite array in the (a) H-plane, (b) E-plane, and (c) D-plane.**

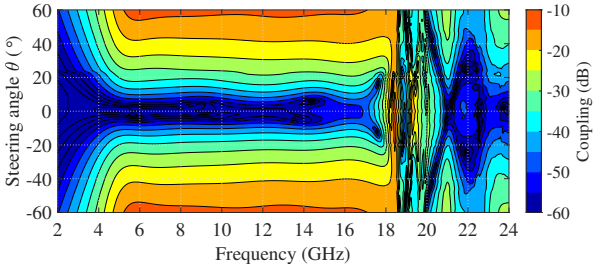

FIGURE 10. **Cross-coupling of the orthogonal polarizations in the unit-cell simulation when the beam is steered in the diagonal plane.**

no indication of scan blindness, which would occur due to surface waves or detrimental resonances in the antenna.

C. FILTERING PERFORMANCE

The filtering performance of the antenna array can be estimated based on the total efficiency computed in the unit-cell simulation. The total efficiency, with respect to the scan angle and frequency, is shown in Fig. 12. The differences between the H-, E-, and D-planes correspond to the differences shown in ARCs [Fig. 9]. They also show that the proposed antenna array element has low resistive losses over the whole beam-steering and frequency range,

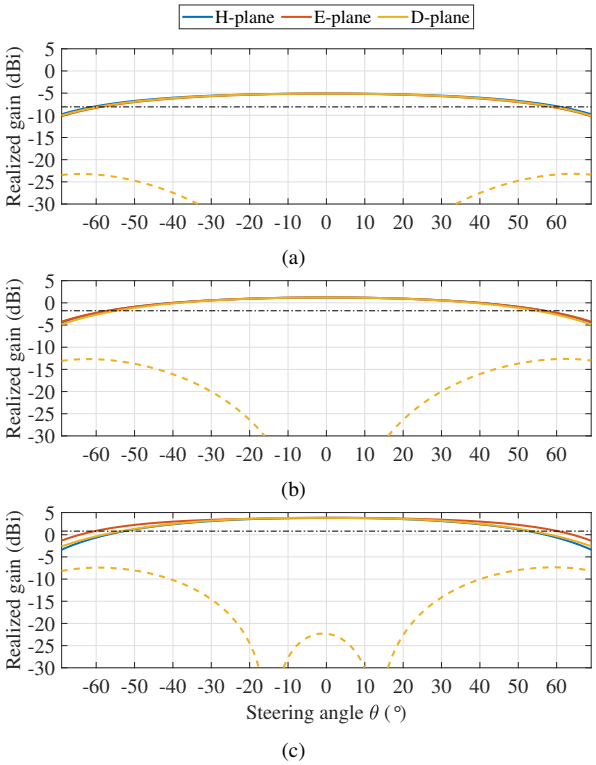

FIGURE 11. **Embedded-element patterns of the infinite array at (a) 6 GHz, (b) 12 GHz, and (c) 18 GHz. Solid lines denote the co-polarized component and the yellow, dashed line is the cross-polarization component in the D-plane ($\phi = 45°$). Black, dashed line shows the 3-dB scan-loss level with respect to the highest realized gain.**

as the total efficiency is mainly better than −1 dB. The maximum total efficiency is slightly better than −0.5 dB in the passband.

The most interesting information in Fig. 12 is the filtering performance in the stopband. Evidently, the transition band from the passband to the stopband is steep as the attenuation increases from 3 dB to 20 dB in a 350-MHz transition band. The stopband attenuation is typically more than 30 dB and at least 20 dB up to 36 GHz if very small areas of lower attenuation at distinct beam-steering angles are ignored. An important observation from these results is that the attenuation of the filter is almost independent of the beam-steering angle.

IV. FULL-ARRAY SIMULATIONS AND MEASUREMENTS

An 11×12 antenna array prototype was manufactured and measured. The prototype array can be considered large at the highest operational frequency (18.5 GHz) and small at the smallest frequency (6 GHz). Consequently, the results from the upper end of the frequency range can be considered to be close to the infinite array predictions, but the lower frequency results may have considerable differences [22].

The antenna array was measured element-by-element when the other ports were terminated to 50-Ω load. The terminations were manufactured by soldering 50-Ω resistors at the end of C.FL cables. The arrangement of the termination

This article has been accepted for publication in IEEE Open Journal of Antennas and Propagation. This is the author's version which has not been fully edited and content may change prior to final publication. Citation information: DOI 10.1109/OJAP.2024.3466234

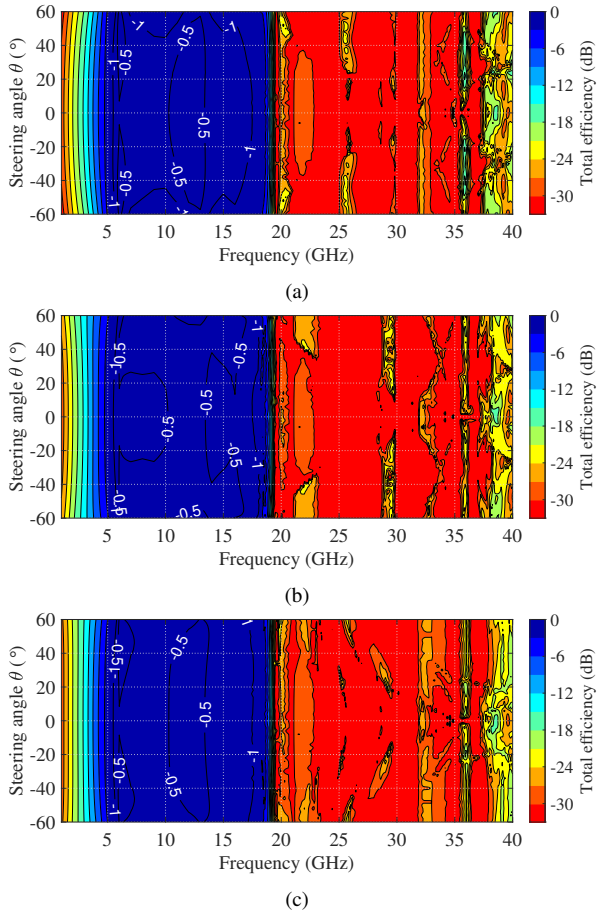

FIGURE 12. Simulated total efficiency of an infinite array in the (a) H-plane, (b) E-plane, and (c) D-plane. Blue color denotes high total efficiency and red color low efficiency (high attenuation).

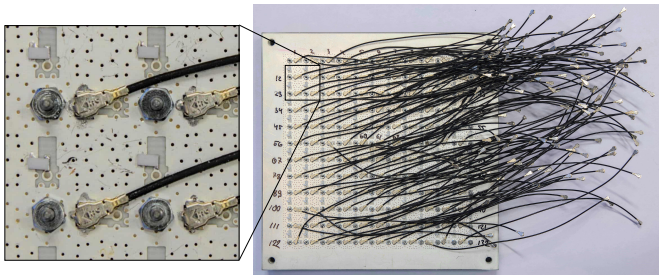

FIGURE 13. Backside of the manufactured antenna array with termination cables.

cables, as well as the backside of the antenna array, is shown in Fig. 13. According to our experiments, the matched load at the end of the C.FL cable provides a termination with a reflection coefficient less than −10 dB in the whole passband.

A. ACTIVE REFLECTION COEFFICIENT AND S-PARAMETERS

S-parameters were measured by a vector network analyzer (VNA) by conducting multiple two-port measurements. All reflection coefficients (diagonal terms) were measured, as well as the coupling of all elements to the center element.

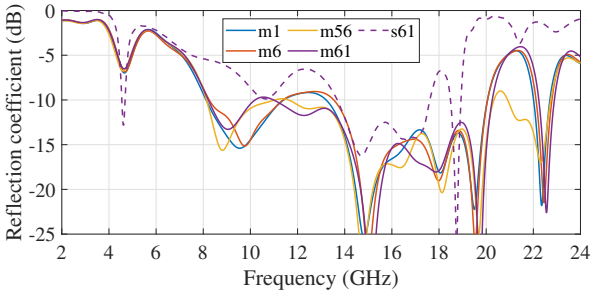

FIGURE 14. Measured (prefix m) and simulated (prefix s) passive reflection coefficients of the representative antenna elements. The element locations are shown in Fig. 16. The measurement data has been time-gated to remove the reflections from the measurement cable and connectors.

This measurement set makes it possible to compute the active reflection coefficient of the center element by combining the effect of other elements when the ports are fed by a uniform feed vector with a progressive phase shifting.

As we used Hirose C.FL [15] connectors, the calibration of the measurement cables was not possible by conventional short-open-load-thru calibration. Thus, the effect of the first reflection from the measurement cable and connectors was removed by time gating the data in MATLAB [23]. However, the time-gating procedure does not compensate for the resistive and mismatch losses of the measurement cable and connectors, which increases from 1.1 dB to 2.2 dB at 5–20 GHz. This will, obviously, improve the ARC and S-parameters accordingly, especially at higher frequencies.

The selected passive S-parameters are shown in Figs. 14 and 15. The port locations are shown in Fig. 16. The reflection coefficients of the center, edge, and corner elements show very uniform behavior, and they correspond to the simulated reflection coefficient of the center element (element 61). However, the level of measured reflection coefficients is considerably lower and the frequency has been shifted. The lower level of reflection obviously comes from the cable loss, whose effect at 20 GHz is about 4.4 dB. Also, coupling coefficients to the adjacent elements and the other center element of orthogonal polarization show very similar behavior if the effect of cable losses is taken into account.

The measured ARC of the center element (element 61) is presented in Fig. 17 in H-, E-, and D-planes. The ARC has been obtained from the time-gated S-parameter data by combining the effect of mutual coupling and reflection coefficient. Progressive phase shifting without any amplitude tapering was used in order to produce easily comparable results. As shown in Fig. 17, the ARC is good from 10 GHz to 20 GHz, but the finite array performs worse than the infinite array model at lower frequencies. This kind of behavior is expectable with finite arrays as the electrical size of the array is smaller at lower frequencies.

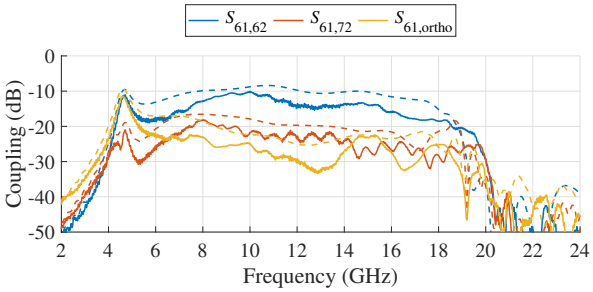

FIGURE 15. **Measured and simulated passive coupling coefficients of the center element, adjacent elements, and other center element of the orthogonal polarization. Simulation results are denoted by dashed lines and measurement results by solid lines.**

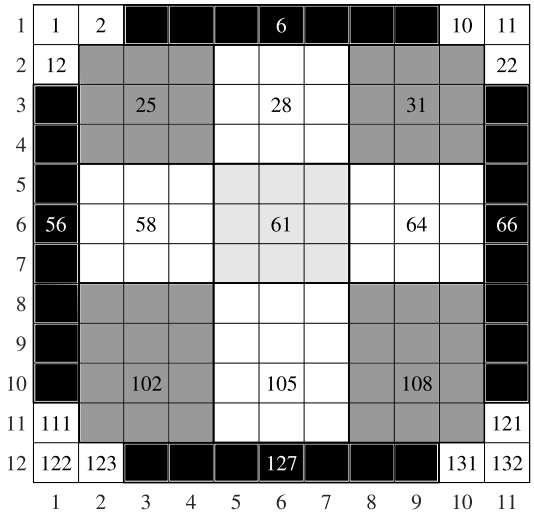

FIGURE 16. **Measured antenna elements and their partitioning in the modified hybrid array-pattern synthesis. The numbers designate the measured antenna elements that have been used to approximate the element pattern of the elements inside the colored box.**

B. EMBEDDED-ELEMENT PATTERNS

The far fields of the selected antenna array elements were measured in the anechoic chamber of Aalto University [Fig. 18] one-by-one. Other elements were terminated with 50-Ω loads soldered to the backside of the PCB and to the ends of the C.FL cables as shown in Fig. 13.

The measured and simulated embedded-element patterns of the center element (element 61) are shown in Figs. 19 and 20. The patterns in the principal and diagonal planes are presented at three different frequencies. The measurement results mainly follow the simulated full-array results. However, at 6 GHz, the fluctuation of the far-field pattern is stronger in the measurements, and it is mainly caused by the behaviour of ARC shown in Fig. 17. In addition, the cross-polarization levels are smaller in the simulations which may imply that the antenna array was unintentionally slightly rotated during the measurements. The measured level of the EEP is larger than in the simulations at 18 GHz, but this effect falls within the error tolerances of the measurement system and simulations. All in all, the measurement results verify that the antenna works as intended.

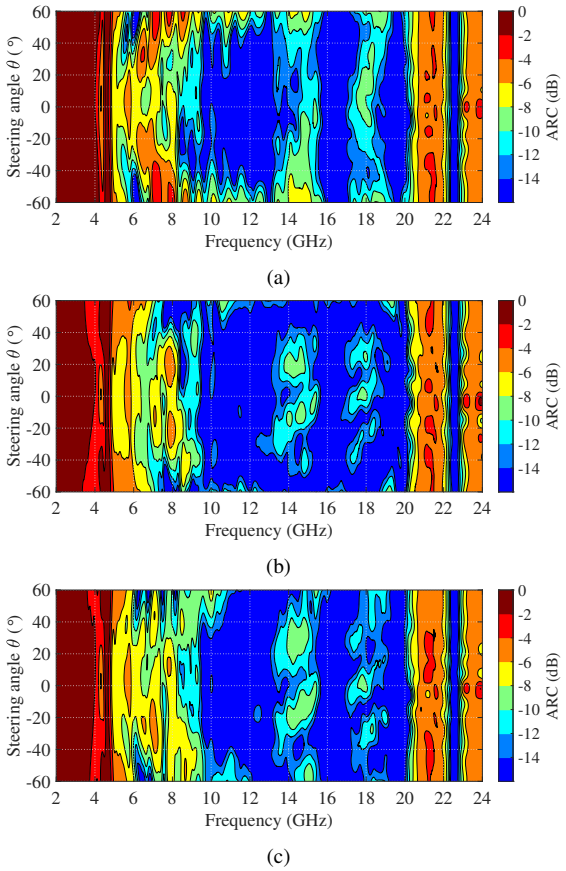

FIGURE 17. **Measured active reflection coefficient of element 61 in the (a) H-plane, (b) E-plane, and (c) D-plane. ARCs have been computed using progressive phase shift and time-gated data.**

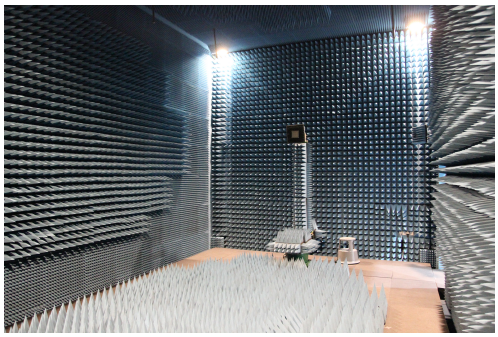

FIGURE 18. **Far-field measurement setup in anechoic chamber of Aalto University. The prototype antenna is installed on the tower. The measurement antenna is in the other end of the room.**

C. SCAN GAIN AND BEAM-STEERING PATTERNS

As one polarization of the manufactured 11×12 array contains 132 antenna elements in total, the measurement of all elements would have been impractical. Thus, a few EEPs were measured, and the scan gain and beam-steering patterns were obtained by combining the measured EEPs using the modified hybrid-AEP method [24]. This method, however, is an approximation and the result may differ from the real beam-steering scenario where all elements are actually fed.

This article has been accepted for publication in IEEE Open Journal of Antennas and Propagation. This is the author's version which has not been fully edited and content may change prior to final publication. Citation information: DOI 10.1109/OJAP.2024.3466234

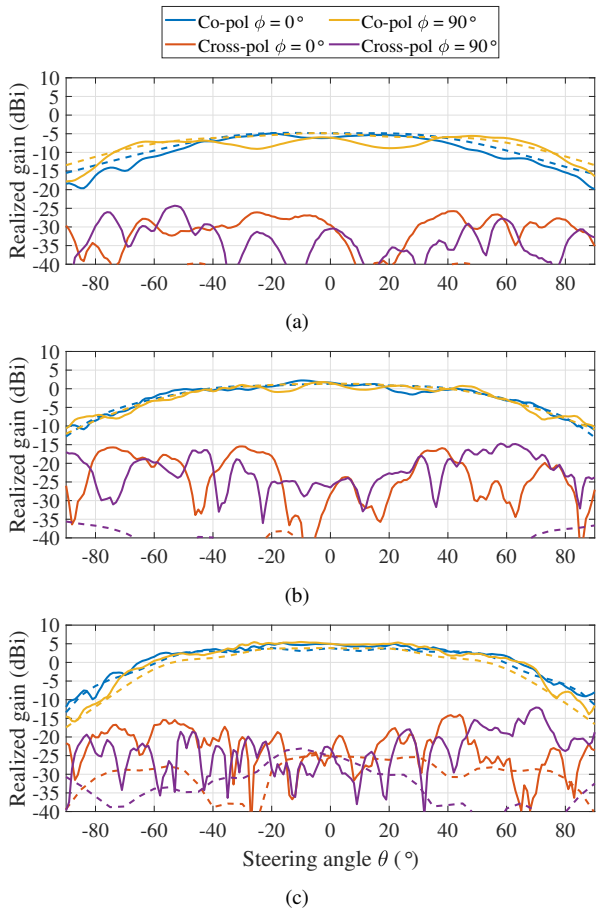

FIGURE 19. Measured (solid line) and simulated (dashed lines) embedded-element patterns of element 61 in the E- ($\phi = 0°$) and H-planes ($\phi = 90°$) at (a) 6 GHz, (b) 12 GHz, and (c) 18 GHz.

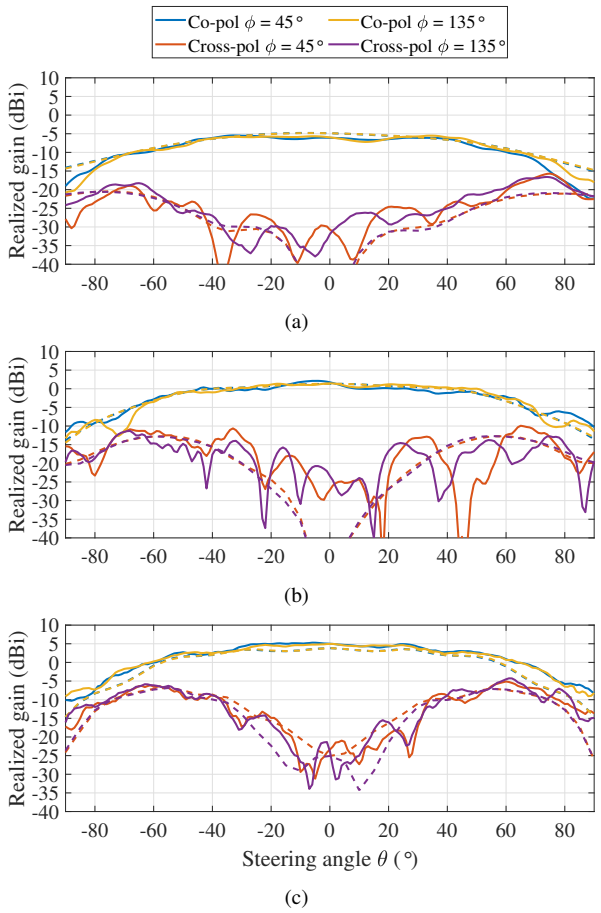

FIGURE 20. Measured (solid line) and simulated (dashed lines) embedded-element patterns of element 61 in both D-planes at (a) 6 GHz, (b) 12 GHz, and (c) 18 GHz.

The partitioning of the antenna elements is shown in Fig. 16. The grid of the figure illustrates the locations of the antenna elements, viewed from the back (connector side). Numbers inside each colored box denote the measured antenna element, and all elements inside that colored box are approximated by that measured antenna element.

According to [24], the total field of the N-element antenna array can be approximated by

$$\boldsymbol{E}(\theta,\phi) = \sum_{n=1}^{N} a_n \boldsymbol{g}_{\mathrm{p}}^{n}(\theta,\phi) e^{jk\hat{\boldsymbol{r}}\cdot\boldsymbol{r}_n}, \tag{2}$$

where $\boldsymbol{g}_{\mathrm{p}}^{n}(\theta,\phi)$ is the phase-adjusted element pattern of element n, a_n is the element excitation coefficient, $\hat{\boldsymbol{r}}$ is the unit vector defining the beam-steering direction, and $\boldsymbol{r}_n$ is the element position vector. The phase-adjusted element patterns are defined by

$$\boldsymbol{g}_{\mathrm{p}}^{n}(\theta,\phi) = \boldsymbol{g}_{\mathrm{m}}^{q}(\theta,\phi) e^{-jk\hat{\boldsymbol{r}}\cdot\boldsymbol{r}_n}, \tag{3}$$

where $\boldsymbol{g}_{\mathrm{m}}^{q}(\theta,\phi)$ is the measured embedded element pattern of element q. For each n, index q is obtained from Fig. 16.

The computed beam-steering patterns are shown in Figs. 21 and 22 for 6 GHz and 18 GHz, respectively. At 6 GHz, the array scans well in the H- and D-planes, but the scan loss is considerably larger, even 5 dB at $\theta = 45°$ in the E-plane. That is, the ARC in the E-plane is worse than in other planes. This kind of behavior is not shown in the unit-cell pattern due to the different ARC at 6 GHz. At larger frequencies, the E-plane scan would be better.

At 18 GHz, the scan pattern follows better the cosine curve. The scan loss is ca. 3 dB in the H-plane and less than 2 dB in the E-plane in $\theta = 45°$ direction. The measured scan loss nearly follows the unit-cell predictions. The small differences are mainly caused by the worse ARC of the measured array elements than that of the unit-cell element.

Fig. 23 shows the normalized maximum realized scan gain with respect to frequency and beam steering angle θ. Normalization of the scan gain is done with respect to the theoretical aperture gain $G_{\mathrm{A}} = 4\pi A_{\mathrm{A}}/\lambda_0^2$, where A_{A} is the area of the aperture. The maximum gain is obtained by taking the maximum realized gain from all θ-angles in that particular scanning plane, and the vertical axis of the figure shows the intended beam-steering direction according to progressive phase shift. This normalization helps to evaluate the filtering performance, total efficiency, and scanning range of the array as it removes the frequency dependency from

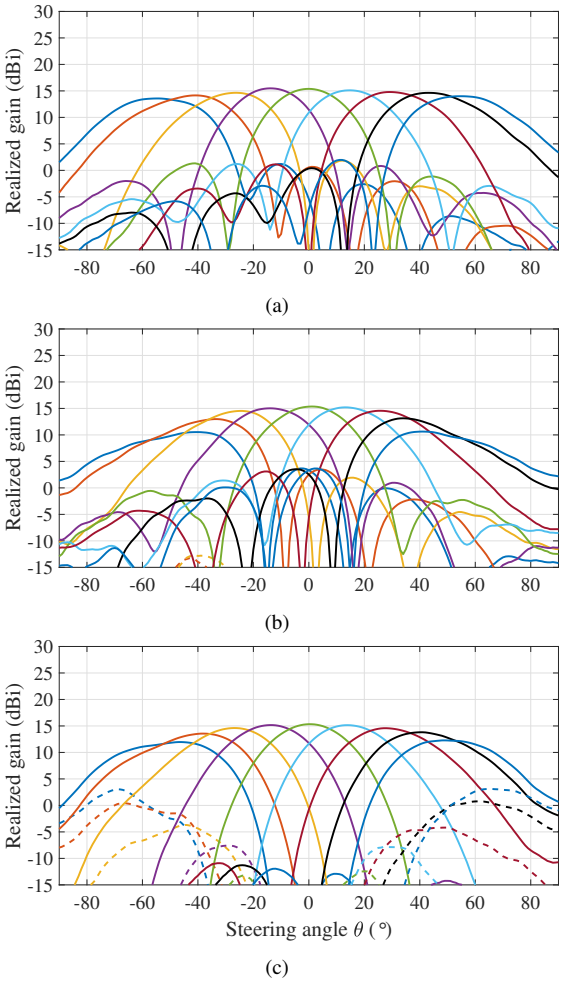

FIGURE 21. Measured beam-steering patterns in the (a) H-plane, (b) E-plane, and (c) D-plane at 6.0 GHz. Progressive phase shift and uniform amplitude distribution were used. Co- and cross-polarized components are drawn by solid and dashed lines, respectively. The radiation patterns are plotted from –60° to 60° with the increment of 15°.

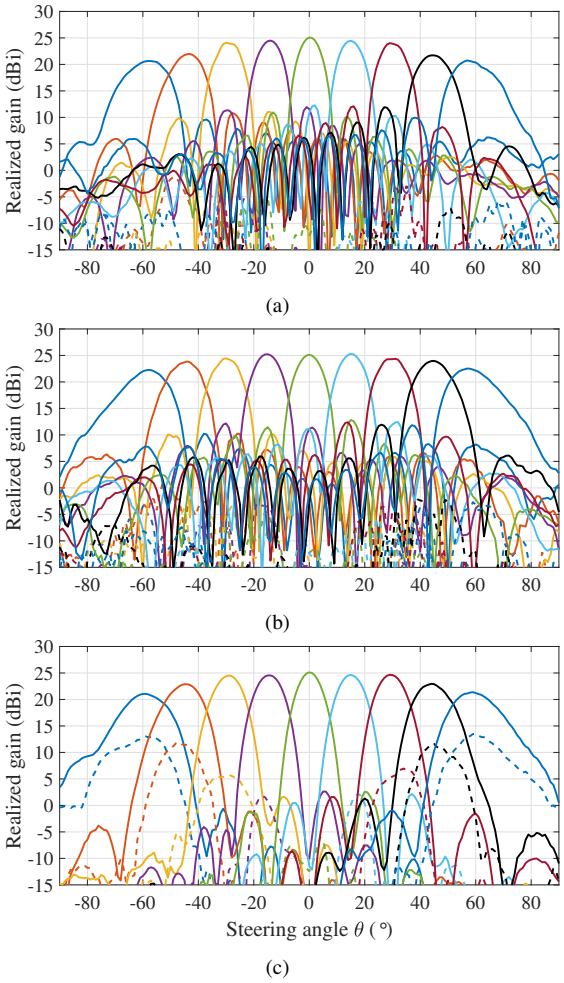

FIGURE 22. Measured beam-steering patterns in the (a) H-plane, (b) E-plane, and (c) D-plane at 18.0 GHz. Progressive phase shift and uniform amplitude distribution were used. Co- and cross-polarized components are drawn by solid and dashed lines, respectively. The radiation patterns are plotted from –60° to 60° with the increment of 15°.

the realized gain. Note that the grating-lobe-free frequency range of the array is up to 18 GHz. Therefore, at higher frequencies, the appearance of grating lobes causes an additional loss of maximum gain. Nevertheless, even if the possible grating lobes are taken into account, Fig. 23 shows an exceptionally wide stopband response, good attenuation, and steep transition band.

The sharpness of the transition band, as well as broadside gain with respect to the frequency, is better illustrated in Fig. 24. Also, the theoretical directivity of the corresponding aperture is shown for comparison. Note that the measured realized gain is slightly larger than the theoretical directivity at certain frequency points since the effective aperture size can be larger than the estimated size.

V. COMPARISON WITH OTHER ANTENNA ARRAYS

A. FILTERING ANTENNA ARRAYS

Table 2 shows a few selected filtering antenna array designs with their performance characteristics for comparison. The other arrays exhibit a band-pass (BP) filtering function instead of low-pass (LP) as they are more common in the literature. In [5], [25]–[27] the filtering arrays have their filters fully integrated into an antenna element (patch or dipole), but in [7], the filtering is done mostly in the feeding network.

The comparison shows that the proposed array has the largest gain suppression level (i.e., out-of-band rejection) and fractional bandwidth (FBW). It should be noted that the majority of the arrays in this comparison were tested only in fixed-beam scenarios. Thus, it is not known how the filter behaves when a progressive phase shift is applied. Furthermore, the proposed array is the largest (11×12) while the other arrays are considerably smaller. In this work, the filtering antenna element has been designed to work in a large array, and thus, also unit-cell simulation results are reported. It is uncertain, how the antenna elements of small arrays behave in a large array.

This article has been accepted for publication in IEEE Open Journal of Antennas and Propagation. This is the author's version which has not been fully edited and content may change prior to final publication. Citation information: DOI 10.1109/OJAP.2024.3466234

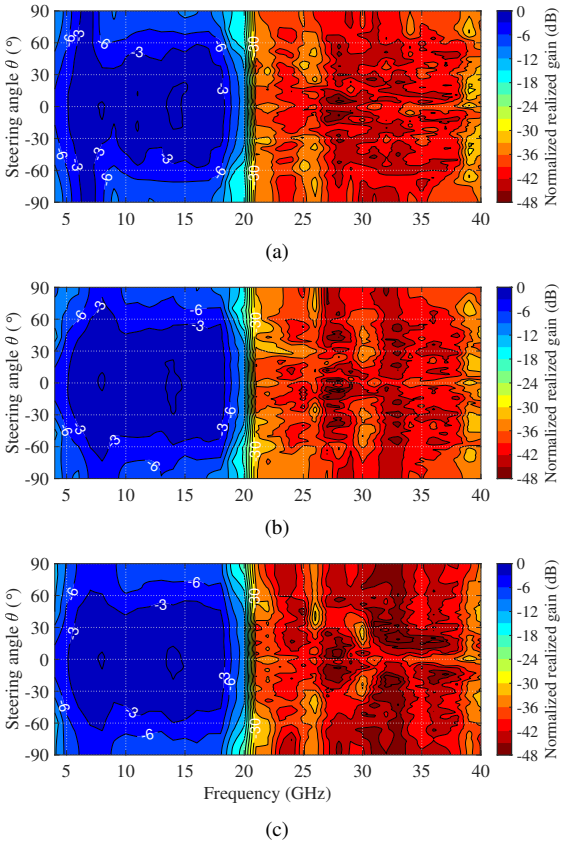

FIGURE 23. **Measured normalized scan gain of the antenna array in the (a) H-plane, (b) E-plane, and (c) D-plane. The normalization is done with respect to the theoretical maximum directivity of the aperture of the equal size.**

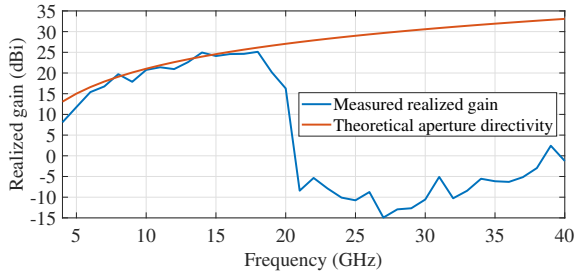

FIGURE 24. **Measured maximum realized gain in the broadside direction and theoretical directivity of a 91.3×99.6 mm aperture.**

However, the proposed array has also some disadvantages. It has a larger profile than others which is a known disadvantage of a Vivaldi element. On the other hand, also the bandwidth becomes higher when increasing the height.

Some designs in Table 2 have a considerably larger inter-element distance than $0.5\lambda_h$, where λ_h is the wavelength in free space at the highest pass-band frequency. These arrays will have grating lobes if the beam is steered too far away from the broadside direction. In the proposed antenna array, the antenna elements with filters can be fitted into $0.5\lambda_h$ lattice.

B. TRADITIONAL VIVALDI ANTENNA ARRAY

The proposed manufacturing technique is also suitable for non-filtering arrays. Thus, the proposed array is qualitatively compared to a traditional Vivaldi array illustrated in Fig. 1 (left side).

1) DESIGN COMPLEXITY

Based on our experience, the design complexity of the proposed antenna array is a bit higher than that of a traditional Vivaldi array. The complexity comes from the expanded design parameters, which include layer count, layer thicknesses, dielectric constants, and perforation of the PCBs. However, these new design parameters give the designer also opportunities to fine-tune the performance for the desired purpose. Electromagnetic modeling of this kind of structure is, of course, more laborious, but not difficult.

2) FABRICATION COST

Fabrication cost of the antenna array consists of PCB fabrication, soldering of components, and assembly. Since PCB fabrication is a highly automated standard process, it will not cost much, especially for large production series. Typically, RF PCBs are not expensive to manufacture since they can be fabricated in standard FR4 process, except PTFE-based laminates like Rogers RT5880. We estimate that due to the larger amount of PCBs, the proposed array will have a larger PCB fabrication cost than a traditional Vivaldi array.

The major cost advantage of the proposed manufacturing method in comparison with a traditional Vivaldi array comes from the assembly. The proposed array contains only planar PCBs that should be placed on each other. The whole stack is then pressed together with screws or other fasteners. Traditional dual-polarized Vivaldi arrays, in turn, use an egg-crate lattice, where multiple PCBs are manually placed across each other. This requires manual assembly, and the PCBs should also be electrically connected. Typically this is done by manual soldering which is time-consuming and costly.

3) ELECTRICAL PERFORMANCE

The performance of the proposed array is comparable to a traditional Vivaldi array if the filtering is not considered. The major difference is that the Vivaldi slot in the proposed array is filled with PCB material. This dielectric loading helps to reduce the height of the element, which causes beneficial effects on cross-polarization and scanning performance. The dielectric layers, however, may cause surface waves that are not a problem with traditional Vivaldi arrays. They can be effectively prevented by perforation, as done in this work.

VI. CONCLUSION

A low-profile filtering antenna array providing a wide operational bandwidth of 6–18.5 GHz and a wide stopband

TABLE 2. Comparison with other filtering antenna arrays.

Ref.	[5]	[7]	[25]	[26]	[27]	[9]	**This work**
Elem. type	Patch	Patch	Patch (LTCC)	Patch	Dipole	Vivaldi	Planar Vivaldi
Filter type	BP, integrated	BP, in feeding network	BP, integrated	BP, integrated	BP, integrated	BP, integrated, periodic TL	LP, integrated, periodic TL
Pass-band FBW	24% (3.3–4.2 GHz)	37% (2.48–3.61 GHz)	20% (24.25–29.5 GHz)	18% (4.5–5.4 GHz)	55% (2.9–5.1 GHz)	88%(1) (1.2–3.1 GHz)	102%(1) (6–18.5 GHz)
Stop-band(2)	4.8–9 GHz	3.9–10 GHz	32–40 GHz	5.7–10 GHz	5.2–6 GHz	3.3–6.0 GHz	21–37 GHz
Gain supp.(3)	>20 dB	18.6 dB	24 dB	13 dB	>11 dB	>20 dB	>30 dB(4)
Total efficiency	NA	>80.3%	87.7% (simulated)	80–94%	NA	50–87%	mainly 80–90%(1)
Polarization	Dual	Single	Dual	Single	Dual	Dual	Dual
Elem. size (λ_h)(5)	0.60x0.81x0.16	0.60x0.84x0.10	0.53x0.53x0.18	0.50x1x0.04	0.97x0.97x0.29	0.52x0.52x1.24	0.51x0.51x0.74
Prototype array size	1×3	2×2	4×4	1×8	1×4	6×6	11×12

(1) Predicted infinite array performance.

(2) Upper stopband with specified gain suppression level, estimated.

(3) Gain suppression with respect to maximum realized gain in passband. Array configuration and broadside beam are assumed. Estimated from measurement results of the upper stopband.

(4) >20 dB up to 40 GHz.

(5) λ_h is the highest operational frequency. First two dimensions define the array lattice, and the last one is the height. In some array designs, the inter-element distance is considerably larger than the size of the actual antenna element.

extending from 19 GHz up to 36 GHz was investigated in this paper. We showed that it is possible to design and manufacture a fully planar Vivaldi-antenna array that is constructed of stacked two-layer PCBs. Only the feed PCB, which includes the balun and connectors, is a multi-layer PCB. The main difference to the known PCB-based Vivaldi array designs is that the radiation direction of the proposed array is perpendicular to the PCB planes.

The advantage of the proposed antenna is a planar structure that can be manufactured using standard PCB manufacturing techniques resulting in a low overall cost. Furthermore, the layered structure inherently supports the design of indentations that were used to realize a high-performance filter inside the Vivaldi slot. The height of the indentations can be easily controlled employing PCBs of different thicknesses.

Furthermore, it is important to note that this stacked-PCB structure can be applied also for conventional, non-filtering arrays. Without the secondary slots inside the Vivaldi slot, the design procedure is even simpler, and higher bandwidths and lower profiles may be possible. In comparison with the other planar, PCB-based arrays, this kind of array probably results in a better beam-steering range as the Vivaldi arrays are generally better than coupled-dipole arrays in the H-plane scan. However, the Vivaldi-antenna-based arrays have also disadvantages, such as generally higher profile and cross-polarization levels than coupled-dipole arrays.

ACKNOWLEDGMENT

The authors would like to thank Mr. Antti Kuhlberg for assisting with the manufacturing of the antenna. This research was conducted in a collaboration between Aalto University and Saab AB. This work was made possible by the research infrastructure provided by Aalto Electronics-ICT.

REFERENCES

[1] F.-C. Chen, J.-F. Chen, Q.-X. Chu, and M. J. Lancaster, "X-band waveguide filtering antenna array with nonuniform feed structure," *IEEE Trans. Microw. Theory Techn.*, vol. 65, no. 12, pp. 4843–4850, Dec. 2017.

[2] C.-X. Mao, S. Gao, Y. Wang, Z. Wang, F. Qin, B. Sanz-Izquierdo, and Q.-X. Chu, "An integrated filtering antenna array with high selectivity and harmonics suppression," *IEEE Trans. Microw. Theory Techn.*, vol. 64, no. 6, pp. 1798–1805, Jun. 2016.

[3] Y. Shi, X. Ni, Z. Qian, S. He, and W. Feng, "Ka-band filtering antenna array based on gap waveguide technology," *IEEE Antennas Wireless Propag. Lett.*, vol. 22, no. 12, pp. 3097–3101, Dec. 2023.

[4] Y. Zhang, X. Y. Zhang, L.-H. Ye, and Y.-M. Pan, "Dual-band base station array using filtering antenna elements for mutual coupling suppression," *IEEE Trans. Antennas Propag.*, vol. 64, no. 8, pp. 3423–3430, Aug. 2016.

[5] K. Xue, D. Yang, C. Guo, H. Zhai, H. Li, and Y. Zeng, "A dual-polarized filtering base-station antenna with compact size for 5G applications," *IEEE Antennas Wireless Propag. Lett.*, vol. 19, no. 8, pp. 1316–1320, Aug. 2020.

[6] M. D. Brown and C. E. Saavedra, "Highly selective and compact filtering antennas using dual-mode SIW resonators," *IEEE Trans. Antennas Propag.*, vol. 71, no. 5, pp. 3928–3937, May 2023.

[7] Y.-M. Zhang, S. Zhang, G. Yang, and G. F. Pedersen, "A wideband filtering antenna array with harmonic suppression," *IEEE Trans. Microw. Theory Techn.*, vol. 68, no. 10, pp. 4327–4339, Oct. 2020.

[8] C.-K. Lin and S.-J. Chung, "A filtering microstrip antenna array," *IEEE Trans. Microw. Theory Techn.*, vol. 59, no. 11, pp. 2856–2863, Nov. 2011.

[9] M. Kuosmanen, J. Holopainen, J. Ala-Laurinaho, T. Kiuru, and V. Viikari, "Filtering antenna array based on corrugated Vivaldi elements," *IEEE Trans. Antennas Propag.*, vol. 71, no. 8, pp. 6546–6557, Aug. 2023.

[10] A. Harvey, "Periodic and guiding structures at microwave frequencies," *IRE Trans. Microw. Theory Techn.*, vol. 8, no. 1, pp. 30–61, Jan. 1960.

[11] R. E. Collin, *Foundations for Microwave Engineering*. New York: McGraw-Hill, 1966.

[12] M. Kuosmanen, S. E. Gunnarsson, J. Malmström, J. Holopainen, J. Ala-Laurinaho, and V. Viikari, "Dual-polarized 6–18-GHz antenna array with low-profile inverted BoR elements," *IEEE Open J. Antennas Propag.*, vol. 4, pp. 3–11, 2023.

[13] X. P. Chen, K. Yang, Q. Q. Shen, and S. Yang Shi, "A wideband phased-array antenna with harmonic suppression based on transformed radial stubs," in *2023 International Conference on Microwave and Millimeter Wave Technology (ICMMT)*, May 2023, pp. 1–3.

[14] W. Yu, H. Lin, B. Liao, and W. Duan, "A compact dual-polarized low-pass filtering antenna with wideband out-of-band rejection," *IEEE Antennas Wireless Propag. Lett.*, vol. 20, no. 12, pp. 2329–2333, Dec. 2021.

[15] HIROSE ELECTRIC CO., LTD., "C.FL series," https://www.hirose.com/product/series/C.FL, (accessed Oct. 20, 2023).

[16] M. Kuosmanen, S. E. Gunnarsson, J. Malmström, H. Kähkönen, J. Holopainen, J. Ala-Laurinaho, and V. Viikari, "Dual-polarized 2–6 GHz antenna array with inverted BoR elements and integrated PCB feed," *IEEE Open J. Antennas Propag.*, vol. 3, pp. 229–237, 2022.

[17] H. Holter, "Dual-polarized broadband array antenna with BOR-elements, mechanical design and measurements," *IEEE Trans. Antennas Propag.*, vol. 55, no. 2, pp. 305–312, Feb. 2007.

[18] S. S. Holland and M. N. Vouvakis, "The planar ultrawideband modular antenna (PUMA) array," *IEEE Trans. Antennas Propag.*, vol. 60, no. 1, pp. 130–140, Jan. 2012.

[19] J. T. Logan, R. W. Kindt, M. Y. Lee, and M. N. Vouvakis, "A new class of planar ultrawideband modular antenna arrays with improved bandwidth," *IEEE Trans. Antennas Propag.*, vol. 66, no. 2, pp. 692–701, Feb. 2018.

[20] J. T. Logan, R. W. Kindt, and M. N. Vouvakis, "Low cross-polarization Vivaldi arrays," *IEEE Trans. Antennas Propag.*, vol. 66, no. 4, pp. 1827–1837, Apr. 2018.

[21] A. Ludwig, "The definition of cross polarization," *IEEE Trans. Antennas Propag.*, vol. 21, no. 1, pp. 116–119, Jan. 1973.

[22] H. Holter and H. Steyskal, "On the size requirement for finite phased-array models," *IEEE Trans. Antennas Propag.*, vol. 50, no. 6, pp. 836–840, Jun. 2002.

[23] B. Archambeault, S. Connor, and J. Diepenbrock, "Time domain gating of frequency domain s-parameter data to remove connector end effects for pcb and cable applications," in *2006 IEEE International Symposium on Electromagnetic Compatibility, 2006. EMC 2006.*, vol. 1, Aug. 2006, pp. 199–202.

[24] D. Kelley and W. Stutzman, "Array antenna pattern modeling methods that include mutual coupling effects," *IEEE Trans. Antennas Propag.*, vol. 41, no. 12, pp. 1625–1632, Dec. 1993.

[25] Y. Zhang, W. Yang, Q. Xue, J. Huang, and W. Che, "Broadband dual-polarized differential-fed filtering antenna array for 5G millimeter-wave applications," *IEEE Trans. Antennas Propag.*, vol. 70, no. 3, pp. 1989–1998, Mar. 2022.

[26] Y.-F. Cheng, Y.-X. Wang, J. Feng, J.-L. Zhong, C. Liao, and X. Ding, "A simple wide-angular scanning phased array with wideband filtering response," *IEEE Trans. Antennas Propag.*, vol. 70, no. 9, pp. 7703–7712, Sep. 2022.

[27] R. Wu, G.-H. Wen, Y. Liu, and F.-C. Chen, "A broadband filtering antenna array for sub-6 GHz base station applications," *IEEE Antennas Wireless Propag. Lett.*, vol. 23, no. 1, pp. 394–398, Jan. 2024.